

# Multi-Layering of Carbon Conductivity Enhancers for Boosting Rapid Recharging Performance of High Mass Loading Lithium Ion Battery Electrodes

Sang Ho Lee<sup>a,\*</sup>, Yige Sun<sup>b</sup> and Patrick S. Grant<sup>b</sup>

<sup>a</sup>Department of Chemical Engineering, Pukyong National University, Busan  
48513, South Korea.

<sup>b</sup>Department of Materials, University of Oxford, Oxford OX1 3PH, UK.

---

\* Address correspondence to sangho.lee@pknu.ac.kr

## **Abstract**

The ability of lithium ion batteries (LIBs) to provide rapid charging characteristics while retaining a substantial energy storage capacity is of paramount significance for their applicability in portable smart electronic devices. In this research, an effective approach to enhance re-charging rates of LIB cells was developed through incorporating carbon nanotube (CNT) conductivity boosters strategically into  $\text{Li}_4\text{Ti}_5\text{O}_{12}$  (LTO) electrodes. A layer-by-layer spray coating was exploited to manufacture multi-layer architectures that comprise sequential, discrete electrode layers of CNT-rich LTO and CNT-free LTO, aiming at promoting charge transfer kinetics of high mass loading electrodes. Initially, the optimal proportion of a CNT-rich layer and its best location within multi-layer electrode structures were investigated in half-cell configurations. The best performing multi-layer was then paired with a spray-coated  $\text{LiFePO}_4$  (LFP) positive electrode in full-cell LIBs, offering attractive power performance of  $\sim 1500$  W/kg that outperformed conventional LTO || LFP combinations.

## **Keywords**

Multi-layering, spray coating, carbon nanotube, rate capability, lithium ion battery.

## 1. Introduction

LIBs have emerged as a prominent and cutting-edge technology due to an increasing demand for wireless power sources for applications in mobile electronics, electric vehicles and ubiquitous computing systems.<sup>[1-4]</sup> Also, there is an ambitious and challenging goal to extend the applicability of LIBs further to aviation industries including passenger aircrafts.<sup>[5,6]</sup> However, to fulfill a wide range of application areas relatively poor LIB's power capability and rapid capacity fade after  $\sim 500$  charge/discharge cycles should be improved while preserving its attractive advantages in gravimetric and volumetric energy storage density with increasing mass loading in electrodes.<sup>[7-10]</sup>

Conventional LIBs comprise two electrodes of anodes and cathodes that are physically and electrically separated by electrolyte/separator. The physical and chemical integrity of the separator and electrolyte has a substantial impact on the safety and susceptibility to failure of LIB systems, whereas deliverable capacity, cell voltage, power performance and cycle life of LIB devices tend to rely on the intrinsic capability of active materials and their spatial arrangement within electrodes.<sup>[11-14]</sup> Particularly, driven by an insight that improving electrical conductivity and ion mobility plays a crucial role in boosting rate capability and cycle stability of high mass loading electrodes, remarkable scientific efforts have been dedicated to not only reducing ohmic resistance in electrodes but also retaining useful electrode pore fractions with an appropriate tortuosity factor.<sup>[15-19]</sup>

From an electrode structure point of view, it typically emphasizes that the local distribution of electrode constituents, such as active materials, carbon conductivity enhancers and polymeric binders, should exhibit uniformity throughout entire electrode structures. However, there is also some counterargument. As electrode

thicknesses and/or effective electrode areas increase gradually, the distribution of conductivity enhancers and/or binders may need to vary correspondingly within electrodes in order to maximize the utilization efficiency of active materials in LIB performance. For example, pouch cell corners that are furthest from the current collector tabs exhibit relatively inefficient utilization of active materials, which was attributed to slow charge transfer kinetics due to long current path through the electrode structure, as reported in literature.<sup>[20-22]</sup> Recently, we have developed graded electrode designs with progressive changes in the concentration of active materials across through-thickness electrodes, leading to marked improvements in overall charge transfer characteristics and C-rate performance of LIB electrodes when compared to conventional electrode configurations with usually uniformly distributed electrode components.<sup>[23,24]</sup>

In this paper, we developed a new and effective approach to improve rate capability and life time of LIB devices. We exploited CNTs as a conductivity booster in order to promote overall charge/discharge dynamics of high mass loading electrodes. A spray coating process was utilized to fabricate multi-layer electrode arrangements comprising discrete layers of CNT-rich LTO and CNT-free LTO, layer-by-layer. The initial step involved the optimization of CNT fractions used in the CNT-rich LTO electrode and its thickness, with the aim of achieving a balance between cost-effectiveness and performance enhancement of CNTs. The most effective location of the CNT-rich layer within the multi-layer electrode was then studied systematically in half-cell configurations, for example placing the CNT-rich layer on the top of the LTO-only layer (closest to the separator and counter electrode), between two layers of LTO-only (a sandwich configuration), and at the LTO-only base (next to the current collector). The best performing multi-layer

electrode structure with the CNT-rich layer deposited on the top of LTO-only was coupled with a spray-coated LFP positive electrode in a full-cell LIB arrangement, offering a specific power density of  $\sim 1500$  W/kg that indicates an approximately 50 % improvement when compared with a conventional CNT-free LIB configuration ( $\sim 1000$  W/kg). The arising multi-layer architecture provides valuable insights into the efficient utilization and distribution of electrode components when designing high mass loading electrodes with attractive energy storage capabilities.

## 2. Experimental section

*Materials:* LTO active materials and carboxymethyl cellulose (CMC) binders were obtained from Sigma Aldrich, UK; CNTs from Thomas Swan & Co. Ltd., UK; Super P (SP) carbon conductivity enhancers from MTI, USA; and LFP active materials from Hydro-Québec, Canada.

*Spray coating process:* For the spray suspension, LTO (or LFP), CNT, SP and CMC in a controlled mass ratio were blended into a 60:40 bi-solvent mixture (by volume) of deionized (DI) water ( $\leq 5 \mu\text{S}/\text{cm}$ ) and isopropyl alcohol (IPA, 99.5 %) using an ultrasonication process. Here, IPA was employed to enhance the effective dispersion of SP and CNT conductivity enhancement materials into the aqueous solution, ensuring the maintenance of the suitably stable and dilute spray suspension ( $\sim 5 \times 10^{-3} \text{ g/mL}$ ). The temperature of the current collector was set at  $120^\circ\text{C}$  in order to facilitate the efficient evaporation of both the IPA and DI water. The atomization of the suspension at the nozzle tip during spray coating was controlled by compressed air pressure in the range of 0.3 to 0.5 bar. The movement speed of the spray scan was adjusted at a constant rate of 2 cm/s. All spray processes were carried out in a fume cupboard.

*Electrochemical characterizations:* The electrochemical behaviors of spray-coated electrodes were investigated using coin-type cells (CR2032) that were assembled in an Ar-filled glovebox ( $\text{H}_2\text{O} < 0.1 \text{ ppm}$ ,  $\text{O}_2 < 0.1 \text{ ppm}$ ). In half-cell tests, lithium foils (99.9% trace metals basis, MTI, USA) were utilized as counter/reference electrodes. For the fabrication of full-cell LIBs, sprayed-coated LTO-based negative electrodes were paired with sprayed-coated LFP positive electrodes. Negative and positive electrodes were electrically separated by a polypropylene separator (Celgard 2400, UK) soaked into 1 M  $\text{LiPF}_6$  electrolyte solution in a 1:1

mixture (by volume) of ethylene carbonate and dimethyl carbonate (Sigma-Aldrich, UK). Charge/discharge performances were analyzed using Arbin BT2000 cyclers at room temperature. Full-cell LIB performances were estimated based on the total weight of negative electrodes including LTO, CNT, SP and CMC. Cyclic voltammetry (CV) and electrochemical impedance spectroscopy (EIS) measurements were carried out using Gamry 600 potentiostats. EIS tests were performed in the range of 1 MHz to 0.1 Hz after the first three CV cycles. The theoretical capacity of LTO and LFP was assumed to be  $\sim 175$  mAh/g and  $\sim 170$  mAh/g, respectively. <sup>[25,26]</sup>

### 3. Results and discussion

This research began with a fundamental inquiry – is the uniform dispersion of carbon-based conductivity enhancers throughout entire electrode structures indeed advantageous for optimizing the potential performance of electrodes? If maintaining the uniform concentration of conductivity enhancement components within electrodes helps to realize the inherent advantages of active materials fully in LIB performance, it could be hypothesized that there is no gradient in the electrochemical behavior of electrodes even as the electrode mass loading and thickness increase incrementally. To investigate changes in electrochemical performances of electrodes as a function of the electrode mass loading and thickness, three electrode configurations with controlled thicknesses of 10, 20 and 40  $\mu\text{m}$  were prepared. All the electrodes were manufactured using an otherwise same spray coating process that allows for the uniform distribution of electrode components throughout electrodes. Here, spinel-type LTO was utilized as an active material because LTO is known to have a zero-strain property and no solid electrolyte interphase formation,<sup>[27,28]</sup> which could contribute greatly to reducing unforeseen side reactions during continuous charge/discharge cycles. Detailed structures of pristine LTO particulates were characterized by scanning electron microscope (SEM) and X-ray diffraction (XRD) measurements, as shown in Figure S1 of the Supporting Information. In the electrode fabrication, a small fraction (5 wt%) of SP conductive carbon particles was employed to precisely monitor variations in the electrochemical behavior of the electrodes in response to changes of the electrode thickness, from 10 to 40  $\mu\text{m}$ . 5 wt% CMC binders were used, so that electrodes were formulated with a 90:5:5 mass ratio of LTO:SP:CMC for all cases, given in Table 1. Figures 1a-c exhibit a series of SEM images for the cross-

sections of 10, 20 and 40  $\mu\text{m}$  spray-coated LTO electrodes, respectively, where the electrode cross-sections were prepared using precision etching and coating system (PECS) process. The magnified SEM image in the inset of Figure 1a represents the surface of the spray-coated LTO electrode, showing a uniform and intertwined configuration of electrode constituents with some degree of porosity.

Figure 1d shows gravimetric discharge capacity retention profiles as a function of C-rates for the same electrodes. Here, the discharge capacity retention was defined as the ratio of the discharge capacities obtained at 0.1, 0.5, 1, 5, 10 and 20 C to the discharge capacity at 0.1 C (refer to Table 1). At relatively low rates of 0.1 to 1 C, all the electrodes had similar capacity retention. However, as C-rates increased gradually to 20 C, the thinnest 10  $\mu\text{m}$  LTO electrode sustained the superior tolerance of  $\sim 80\%$ , whereas the 40  $\mu\text{m}$  electrode had capacity retention reduced to  $\sim 50\%$ . In Figure 1e, the cycle life was further examined at a constant charge/discharge rate of 1 C. After 300 cycles, the 10  $\mu\text{m}$  LTO electrode was shown to retain a stable capacity of  $\sim 130\text{ mAh/g}$ , but the initial capacity of the 40  $\mu\text{m}$  electrode was collapsed catastrophically to  $\sim 70\text{ mAh/g}$ . EIS measurements were then carried out to study charge transfer characteristics for the identical electrodes (inset). As electrode thicknesses increased from 10 to 40  $\mu\text{m}$ , the size of semi-circles increased exponentially, indicating the increase in overall ohmic resistance in the electrode. It concluded that the usually uniform dispersion of conductivity enhancers throughout the entire electrode caused “useless” through-thickness gradients in charge transfer resistance as the electrode mass loading and thickness increased, which then resulted in “unwanted” electrode capacity collapses at high C-rates and over repeated charge/discharge cycles.

To mitigate the development of a through-thickness impedance gradient with increasing electrode thicknesses, we exploited a stepwise multi-layering approach, with the intention to re-distribute carbon conductivity enhancer fractions strategically within electrode structures. Figure 2 shows a schematic for the fabrication of a multi-layer architecture by spray coating using switching between suspension feedstocks at will. For example, two types of spray suspensions were prepared: (i) the CNT-free LTO suspension solution (yellow) that was formulated with a 90:5:5 mass ratio of LTO:SP:CMC; and (ii) the CNT-rich LTO suspension (blue) in which a controlled fraction of CNTs was blended into LTO-based solution. A photography in Figure S2 of the Supporting Information shows the CNT-rich LTO suspension, demonstrating the absence of sedimentation and settling of the solid electrode constituents. Here, CNTs were utilized as an additional conductivity booster to explore the impact of the re-arrangement of conductivity enhancement components on electrochemical performances of high mass loading electrodes (Figure S3 in the Supporting Information presents SEM and Raman spectroscopy data for pristine CNT materials). It is well known that CNTs have the excellent electrical conductivity as well as facilitate the formation of beneficial networks between electrode components, providing additional functionality and performance improvements in a wide range of device applications.<sup>[29-32]</sup> Particularly, various types of CNT materials have been utilized as conductive additives in the manufacture of LIB electrodes. However, most of CNT additives in the literature have been typically blended and uniformly dispersed alongside other constituents within electrode structures.<sup>[33-35]</sup>

The successful fabrication of the multi-layer architecture involves employing a heated current collector. Prior to the spray coating process, the current collector was

fixed on a vacuum chuck of a hot plate that was then heated to a pre-set temperature ( $> 100\text{ }^{\circ}\text{C}$ ). The heated current collector allowed for fast drying of sprayed droplets onto the current collector and the successive superimposition of sub-layers over the pre-formed layer with a minimum inter-mixing between inter-layers. The cone-shaped spray then moved back and forth over the heated current collector according to the pre-programmed zig-zag path in the  $x$  and  $y$  direction with a fixed spray distance  $z$ . The reciprocating motion of the spray nozzle for multiple cycles ensures even and uniform coverage of electrode constituents on the entire area of the current collector. By the iterative process of conducting spray scan cycles, the electrode layer can be incrementally constructed to the desired thickness, resulting in precise control over the electrode thickness. Furthermore, the effective electrode area can be modified simply through adjusting the movement range of the spray scan.

Initially, to optimize the proportion of CNTs used in the CNT-rich layer, the electrochemical behaviors for  $40\text{ }\mu\text{m}$  thick spray-coated electrodes of random mixtures of LTO and CNT were investigated as a function of CNT weight fractions, in the range of 0 to 20 wt%, as shown in Figure S4 of the Supporting Information. As CNT fractions within electrodes increased progressively from 0 to 20 wt%, LTO fractions decreased inversely from 90 to 70 wt%, as shown in comparative bar graphs in Figure S4a. Here, the weight fraction of SP and CMC within the CNT-rich layer was fixed at 5 wt%, respectively, given in Table S1 of the Supporting Information. Figure S4b shows the electrochemical behavior of LTO electrodes as a function of CNT fractions at increasing rates of 0.1 to 20 C. It should note that discharge capacities of electrodes were estimated on the basis of the total electrode mass including LTO, CNT, SP and CMC. In the range of 0.1 to 5 C, the CNT-free LTO-only electrode delivered superior discharge capacities to the CNT-rich LTO

electrodes, implying that CNT additives contributed only to a parasitic mass in deliverable capacity estimation when charge/discharge dynamics in the electrode remained relatively unaffected by rapid charge transfer characteristics. However, at higher rates of 10 C and 20 C the CNT-rich LTO electrodes overwhelmed the LTO-only equivalent in terms of deliverable capacities. Particularly, the 10 wt% CNT electrode had the highest capacity of  $\sim 100$  mAh/g at 20 C, given in Table S1. In Figure S4c, CV profiles for the same electrodes present a pair of anodic/cathodic peaks at approximately 1.7 V/1.5 V, typical of spinel-type LTO.<sup>[36,37]</sup> The absence of noticeable peak shifts in the CV curves suggests that the addition of CNT conductivity boosters did not significantly affect the electrochemical behavior of LTO. The Nyquist curves in Figure S4d show an exponential decrease in charge transfer resistance of the electrodes as CNT fractions within electrodes increased progressively. Overall, when evaluating the balance between cost-efficiency and rate performance enhancement in electrode design, a composition of 10 wt% CNTs were selected as the preferred choice for use in the CNT-rich layer, and then sequentially studied to optimize microstructures in multi-layer electrodes. SEM images in Figure S5 of the Supporting Information present the surface of the spray-coated 10 wt% CNT-rich electrode, indicating that CNTs were uniformly dispersed and entangled with agglomerates of LTO and SP within the electrode structure.

To quantify an optimum thickness of the CNT-rich layer within 40  $\mu\text{m}$  thick multi-layers, four electrodes with the controlled thickness of the CNT-rich layer, in the range of 10 to 40  $\mu\text{m}$ , were prepared. For the multi-layer fabrication, a CNT-free LTO-only electrode layer was first formed on the current collector, followed by the successive deposition of a CNT-rich layer on the pre-formed LTO-only layer, as described in the scheme in Figure 2. Figures 3a-d exhibit a series of SEM images

for the cross-section of the multi-layer electrodes. As the thickness of CNT-rich layers increased progressively from 10 to 40  $\mu\text{m}$ , the LTO-only layer thickness within the multi-layer decreased correspondingly from 30 to 0  $\mu\text{m}$ . In Figure S6 of the Supporting Information, energy-dispersive X-ray spectroscopy (EDS) line scanning profiles (for carbon) verify the variation in the thickness of the CNT-rich layer within the multi-layers.

Figure 3e shows gravimetric discharge capacity profiles at increasing C-rates for the same electrodes. In the range of 0.1 to 2 C, the multi-layer electrode with the 10  $\mu\text{m}$  CNT-rich layer had the highest discharge capacities. However, at 20 C the highest discharge capacity of the 10  $\mu\text{m}$  CNT-rich layer reduced to  $\sim 80$  mAh/g that was even lower than that of the 40  $\mu\text{m}$  CNT-rich layer. By contrast, the multi-layer structure with the 20  $\mu\text{m}$  CNT-rich layer retained the highest discharge capacity of  $\sim 100$  mAh/g at 20 C (refer to Table 2). The inset bar graph summarizes the variation of deliverable discharge capacities at 0.1 C and 20 C for the same multi-layer electrodes. Figure 3f shows galvanostatic discharge capacity profiles at a constant charge/discharge rate of 2 C. As charge/discharge cycles progressed to the 300<sup>th</sup> cycle, the multi-layer with the 20  $\mu\text{m}$  CNT-rich layer sustained the highest discharge capacity of  $\sim 100$  mAh/g, corresponding to  $\sim 75$  % capacity retention (see Figure S7 in the Supporting Information). On the contrary, the highest initial capacity of the 10  $\mu\text{m}$  CNT-rich layer was rapidly dropped after 150 cycles, resulting in the lowest capacity retention of  $\sim 60$  % at the 300<sup>th</sup> cycle. The 40  $\mu\text{m}$  CNT-rich layer had the highest capacity retention of  $\sim 80$  % because a comparatively low initial capacity was well sustained after 300 cycles. All the electrodes sustained almost 100 % coulombic efficiency after 300 cycles, excluding the first few cycles, as shown in the Figure S8 of the Supporting Information. The

Nyquist curves (inset) show a progressive decrease in overall charge transfer resistance with increasing the CNT-rich layer thickness, from 10 to 40  $\mu\text{m}$ . As a result, it suggested an insight that adding CNT conductivity boosters was unarguably advantageous for reducing ohmic resistance within electrodes, but their excessive use resulted in a reduction in the overall electrode capacity because they contributed to only a worthless weight in the actual capacity estimation. Thus, using the multi-layer configuration with the 20  $\mu\text{m}$  CNT-rich layer further explorations were carried out in order to enhance the rate capability and cycle stability of LIB electrodes.

To investigate if extra benefits to electrode performance are potentially achievable by spatial variations of microstructures in electrodes, the electrochemical behavior was examined systematically according to changes in the location of the 20  $\mu\text{m}$  CNT-rich layer within multi-layers. Figures 4a-c exhibit a series of concentric back scattered (CBS) images for the cross-section of arising stepwise multi-layers: locating the 20  $\mu\text{m}$  CNT-rich layer (a) on the top of the LTO-only layer (near the separator, denoted as LTO-CNT); (b) between two layers of LTO-only (a sandwich configuration, LTO-CNT-LTO); and (c) at the base of LTO-only (next to the current collector, CNT-LTO). The overall electrode thickness was maintained constantly at 40  $\mu\text{m}$  for all cases, sustaining almost same electrode mass loading, given in Table 3. Figures 4d-f show corresponding EDS elemental map images for carbon (red), representing the spatial re-alignment of the 20  $\mu\text{m}$  CNT-rich layer within the 40  $\mu\text{m}$  multi-layer at will.

Figure 5a shows gravimetric discharge capacity profiles of the same electrodes as a function of C-rates. In the range of 0.1 to 0.5 C, the spatial variation of the CNT-rich layer made little difference in electrode capacities. However, as C-rates

increased further to 20 °C the LTO-CNT multi-layer configuration had the highest deliverable capacity of ~ 100 mAh/g and the best capacity retention of ~ 75 % (see Figure S9 in the Supporting Information), which was also superior to an electrode of uniformly mixed LTO and CNT particulates in the same combination of 85 wt% LTO and 5 wt% CNT (on the basis of the total electrode weight), as presented in Figure S10 of the Supporting Information.

It could be hypothesized that if the composition of conductivity enhancers is uniformly dispersed throughout a thick and high mass loading electrode, a through-thickness gradient of charge transfer resistance develops progressively from the electrode/current collector interface towards the region of the electrode distant from the current collector. In principle, interleaving highly conductive materials, such as metals or metal alloys, at the interface between the current collector and electrode may become an effective approach to delay the onset of an unhelpful through-thickness impedance gradient. Alternatively, increasing the proportion of conductivity enhancement components at the electrode region distant from the current collector (e.g. near the separator) could also help reduce the overall electrode impedance. The inset in Figure 5a shows Nyquist curves for the identical multi-layer electrode structures, representing the variation in charge transfer resistance as a function of the spatial re-arrangement of the CNT-rich layer. The LTO-CNT multi-layer configuration had the lowest electrochemical impedance value. It implies that the incorporation of a small quantity of CNT additives and strategically placing the CNT-rich layer near the separator were shown to provide substantial advantages in enhancing the charge transfer kinetics of electrode structures.

Figure 5b shows volumetric discharge capacity profiles and corresponding capacity retentions at a constant charge/discharge rate of 2 C. Here, volumetric capacity values were calculated by dividing the resulting gravimetric capacities by the electrode mass loading and thickness (Table 3). After 300 cycles, the LTO-CNT arrangement had superior volumetric capacity ( $\sim 120 \text{ mAh/cm}^3$ ) and corresponding capacity retention ( $\sim 80 \%$ ) to the LTO-CNT-LTO and CNT-LTO equivalents. Regardless of changes in the placement of the CNT-rich layer, all the multi-layer electrodes had almost 100 % coulombic efficiency after 300 cycles, as shown in the Figure S11 of the Supporting Information.

Given that an improvement in charge transfer characteristics of LIB electrodes is known to have a great influence on lithium ion intercalation kinetics, the effective ion mobility was further investigated as a function of the microstructure variation in the multi-layers. Figures 6a-c show the change in anodic/cathodic peak current densities as a function of CV scan rates in the range of 0.05 to 1.00 mV/s for the LTO-CNT, CNT-LTO and LTO-only electrodes, respectively. As the scan rate increased to 1.00 mV/s, the anodic/cathodic peaks at approximately 1.7 V/1.5 V increased proportionally for all the electrode cases. However, the extent of anodic/cathodic current density increases was shown to rely on microstructure variations within the electrodes. For example, with increasing scan rates the peak intensity of the LTO-CNT arrangement increased more markedly when compared with that of the CNT-LTO and LTO-only electrodes. In Figure 6d, the increasing tendency of the anode peak current densities at approximately 1.7 V shows a good linear fit to the square root of the scan rate, implying that the effective lithium ion mobility within the electrodes could be estimated using the Randles-Sevcik equation.<sup>[38,39]</sup>

$$I_p = 0.4463n F A C_0 (n F v M_{Li} / RT)^{1/2} \quad (1)$$

where  $I_p$  was the anode peak current density [A],  $n$  was the number of electrons transferred during the charge/discharge reaction,  $F$  was the Faraday constant [C/mol],  $A$  was the effective electrode area [cm<sup>2</sup>],  $C_0$  was the molar density of the lithium ions in the electrode [mol/cm<sup>3</sup>],  $v$  was the scan rate [V/s],  $M_{Li}$  was the ion mobility [cm<sup>2</sup>/s],  $R$  was the gas constant [J/K·mol] and  $T$  was temperature [K].

In general, the Randles-Sevcik equation is applied to better understand the ion mobility or diffusive behavior within electrodes according to types of electrode materials or their spatial variation.<sup>[40-42]</sup> However, as the measurement and its corresponding interpretation require particular caution and precision, we have taken meticulous measures to ensure that the mass loading, thickness and composition of the electrodes were otherwise identical. Thus, the variation of electrode microstructures (e.g. the LTO-CNT and CNT-LTO configurations) was the only factor to affect the lithium ion mobility, ensuring the effect and the appropriateness of this investigation.

The bar graphs in Figure 6e summarize the effective ion mobility estimation as a function of the spatial re-arrangement of the CNT-rich layer. The LTO-CNT configuration had the highest lithium ion mobility of  $\sim 3.1 \times 10^{-11}$  cm<sup>2</sup>/s, which outperformed the CNT-LTO ( $M_{Li} \sim 2.3 \times 10^{-11}$  cm<sup>2</sup>/s) and LTO-only ( $M_{Li} \sim 1.6 \times 10^{-11}$  cm<sup>2</sup>/s) equivalents. Overall, the increase in ion diffusion characteristics was shown to be predominantly derived from the adequate re-distribution of conductive enhancer fractions, making improvements in electrode charge/discharge dynamics.

Figure 6f represents the double-sided fabrication of the spray-coated LTO-CNT multi-layer architecture over a 20 cm × 20 cm Cu current collector foil, suggesting

the potential for scalability to applications for the manufacture of pouch cell-type LIB configurations that are promisingly applicable for hybrid/pure electric vehicles and grid-scale stationary energy storage systems.

The benefits of the enabling multi-layer electrode structure were further investigated in full-cell LIB types. The best performing LTO-CNT negative electrode was coupled with a spray-coated LFP positive electrode in a full-cell arrangement (hereafter denoted as LTO-CNT LIB). A similar LIB arrangement comprising a CNT-free LTO-only negative electrode and a LFP positive electrode was also prepared for comparison (denoted as LTO-only LIB). All the LIBs were formulated with an anode:cathode capacity ratio of approximately 1:1, given in Table 4. Note that Figure S12 and Table S2 in the Supporting Information provide half-cell performances of spray-coated LFP positive electrodes. Figure 7a shows LIB energy density profiles as a function of C-rates. At relatively low rates of 0.1 C and 0.5 C, the LTO-CNT multi-layer electrode made little difference in LIB energy density performance, e.g. with energy density of  $\sim 300$  Wh/kg at 0.1 C for both the LIB configurations. However, a gap in deliverable energy density values between the LTO-CNT and LTO-only LIBs became more marked as C-rates increased progressively to 10 C. For instance, the LTO-CNT LIB had superior power density of  $\sim 1500$  W/kg at 10 C, as shown in Ragone plots (inset), corresponding to an approximately 50 % improvement in gravimetric power performance when compared with the LTO-only LIB ( $\sim 1000$  W/kg).

Figure 7b shows volumetric charge/discharge curves of the identical LIBs at increasing C-rates, where the volumetric capacity values were re-estimated by normalizing the gravimetric capacity data by the mass and thickness of anode electrodes, given in Table 4. At 0.1 C, the LTO-CNT configuration had slightly

lower volumetric capacity of  $\sim 165 \text{ mAh/cm}^3$  than the LTO-only LIB equivalent ( $\sim 175 \text{ mAh/cm}^3$ ), which was associated with high volume of CNT additives per unit mass. However, as C-rates increased further to 10 C, the LTO-CNT LIB configuration had an approximately 60 % improvement in deliverable volumetric capacity compared with the LTO-only LIB.

Figure 7c shows gravimetric discharge energy density profiles at a constant charge/discharge rate of 2 C as a function of continuous charge/discharge cycles. After 500 cycles, the LTO-CNT LIB delivered an attractive discharge energy density of  $\sim 180 \text{ Wh/kg}$  that corresponded to  $\sim 80 \%$  of the initial energy density (the right-hand inset), while the conventional LTO-only LIB had energy density reduced to  $\sim 110 \text{ Wh/kg}$ , corresponding to  $\sim 65 \%$  retention (the right-hand inset). The left-hand inset represents a schematic illustration for the best performing LTO-CNT || LFP arrangement in a full-cell LIB.

#### 4. Conclusions

Through-thickness multi-layer structures with stepwise grading of CNT additive fractions were developed to boost the electrochemical energy storage capacity of high mass loading electrodes at high C-rates and over repeated charge/discharge cycles. The optimum proportion of the CNT-rich layer and its best position within the multi-layer were investigated systematically in half-cell configurations. The best performing multi-layer electrode then provided significant performance enhancements in full-cell LIB devices, with energy density of  $\sim 300$  Wh/kg and power density of  $\sim 1500$  W/kg.

The bespoke multi-layering approach holds the potential to become a cutting-edge technology that offers remarkable flexibility in exploring and customizing the electrochemical behavior of electrodes based on variations in electrode microstructures, spatial alignments and composition distributions. Strategically redistributing conductivity enhancement materials in through-thickness and/or in-plane directions within electrodes could provide a promising model for designing a “smart” electrode architecture that capitalizes on the inherent properties of active materials and prioritizes rapid electrochemical responses, advancing the ultimate technology of electrochemical lithium ion storage systems.

## Acknowledgments

This work was supported by the UK Faraday Institution through grant NEXTRODE - Next generation electrodes number (FIRG015), the National Research Foundation of Korea grant (NRF-2021R1C1C2013340) and the Technology Innovation Program (20019249) funded By the Ministry of Trade, Industry & Energy (MOTIE, Korea). The authors would like to thank Hydro-Québec for providing LiFePO<sub>4</sub>.

## References

1. Z. Qi, J. Tang, S. Misra, C. Fan, P. Lu, J. Jian, Z. He, V. G. Pol, X. Zhang, H. Wang, *Nano Energy* 69 (2020) 104381.
2. M. Winter, B. Barnett, K. Xu, *Chem. Rev.* 118 (2018) 11433-11456.
3. X. Zhou, L. Yu, X. -Y. Yu, X. W. Lou, *Adv. Energy Mater.* 6 (2016) 1601177.
4. S. H. Lee, *Batteries & Supercaps* 6 (2022) e202200380.
5. O. Yetik, T. H. Karakoc, *Energy* 195 (2020) 117009.
6. A. Nishizawa, J. Kallo, O. Garrot, J. Weiss-Ungethüm, *J. Power Sources* 222 (2020) 294-300.
7. S. H. Lee, C. Huang, P. S. Grant, *Energy Storage Mater.* 38 (2021) 70-79.
8. M. Li, J. Lu, Z. Chen, K. Amine, *Adv. Mater.* 30 (2018) 1800561.
9. A. I. Inamdar, R. S. Kalubarme, J. Kim, Y. Jo, H. Woo, S. Cho, S. M. Pawar, C. -J. Park, Y. -W. Lee, J. I. Sohn, S. Cha, J. Kwak, H. Kim, H. Im, *J. Mater. Chem. A* 4 (2016) 4691-4699.
10. M. Kim, S. K. Kang, J. Choi, H. Ahn, J. Ji, S. H. Lee, W. B. Kim, *Nano Lett.* 22 (2022) 10232-10239.
11. C. Huanga, N. P. Young, J. Zhang, H. J. Snaith, P. S. Grant, *Nano Energy* 31 (2017) 337-385.

12. J. Xie, J. Wang, H. R. Lee, K. Yan, Y. Li, F. Shi, W. Huang, A. Pei, G. Chen, R. Subbaraman, J. Christensen, Y. Cui, *Sci. adv.* 4 (2018) eaat5168.
13. S. H. Lee, Y. -R. Jo, Y. Noh, B. -J. Kim, W. B. Kim, *J. Power Sources* 367 (2017) 1-7.
14. D. Lin, Y. Liu, Y. Cui, *Nat. Nanotechnol.* 12 (2017) 194-206.
15. Z. Chen, D. L. Danilov, R. -A. Eichel, P. H. L. Notten, *Adv. Energy Mater.* 12 (2022) 2201506.
16. Z. Li, J. Liu, Y. Qin, T. Gao, *ACS Appl. Mater. Interfaces* 14 (2022) 33004-33012.
17. J. P. Pender, G. Jha, D. H. Youn, J. M. Ziegler, I. Andoni, E. J. Choi, A. Heller, B. S. Dunn, P. S. Weiss, R. M. Penner, C. B. Mullins, *ACS Nano* 14 (2020) 1243-1295.
18. S. H. Lee, Y. Noh, Y. -R. Jo, Y. Kim, B. -J. Kim, W. B. Kim, *Energy Technol.* 6 (2018) 1255-1260.
19. S. H. Lee, C. Johnston, P. S. Grant, *ACS Appl. Mater. Interfaces* 11 (2019) 37859-37866.
20. E. Hosseinzadeh, R. Genieser, D. Worwood, A. Barai, J. Marco, P. Jennings, *J. Power Sources* 382 (2018) 77-94.
21. S. J. Bazinski, X. Wang, *J. Electrochem. Soc.* 161 (2014) A2168-A2174.
22. L. Cai, K. An, Z. Feng, C. Liang, S. J. Harris, *J. Power Sources* 236 (2013) 163-168.
23. C. Cheng, R. Drummond, S. R. Duncan, P. S. Grant, *J. Power Sources* 448 (2020) 227376.
24. C. Cheng, R. Drummond, S. R. Duncan, P. S. Grant, *J. Power Sources* 413 (2019) 59-67.

25. S. H. Lee, C. Huang, P. S. Grant, *Energy Storage Mater.* 38 (2021) 70-79.
26. S. H. Lee, K. Li, C. Huang, J. D. Evans, P. S. Grant, *ACS Appl. Mater. Interfaces* 11 (2019) 603-612.
27. C. Han, Y. –B. He, M. Liu, B. Li, Q. –H. Yang, C. –P. Wong, F. Kang, *J. Mater. Chem. A* 5 (2017) 6368-6381.
28. L. Wu, X. Leng, Y. Liu, S. Wei, C. Li, G. Wang, J. Lian, Q. Jiang, A. Nie, T. –Y. Zhang, *ACS Appl. Mater. Interfaces* 9 (2017) 4649-4657.
29. J. Jing, K. Liu, J. Jiang, T. Xu, S. Wang, J. Ma, Z. Zhang, W. Zhang, T. Liu, *Photonics Res.* 10 (2022) 126-147.
30. X. Zhao, H. Jin, J. Liu, J. Chao, T. Liu, H. Zhang, G. Wang, W. Lyu, S. Wageh, O. A. Al-Hartomy, A. G. Al-Sehemi, B. Fu, H. Zhang, *Laser Photonics Rev.* 16 (2022) 2200386.
31. J. Zhu, R. Bernhardt, W. Cui, R. German, J. Wagner, B. V. Senkovskiy, A. Grüneis, T. Pichler, Y. Li, X. Li, K. Wu, R. Liu, X. Zhu, P. H. M. V. Loosdrecht, L. Shi, *Laser Photonics Rev.* 15 (2021) 2100259.
32. S. H. Lee, C. Huang, C. Johnston, P. S. Grant, *Electrochim. Acta* 292 (2018) 546-557.
33. B. J. Landi, M. J. Ganter, C. D. Cress, R. A. DiLeo, R. P. Raffaele, *Energy Environ. Sci.* 2 (2009) 638-654.
34. J. H. Choi, C. Lee, S. Park, M. Hwang, T. J. Embleton, K. Ko, M. Jo, K. S. Saqib, J. Yun, M. Jo, Y. Son, P. Oh, *Electrochem. Commun.* 146 (2023) 107419.
35. J. Kirner, Y. Qin, L. Zhang, A. Jansen, W. Lu, *J. Power Sources* 450 (2020) 227711.

36. A. Lakshmi-Narayana, M. Dhananjaya, C. M. Julien, S. W. Joo, C. V. Ramana, *ACS Appl. Mater. Interfaces* 15 (2023) 20925-20945.
37. S. H. Lee, C. Johnston, P. S. Grant, *Energy. Technol.* 8 (2020) 2000253.
38. S. H. Lee, A. Mahadevegowda, C. Huang, J. D. Evans, P. S. Grant, *J. Mater. Chem. A* 6 (2018) 13133-13141.
39. Y. J. Kim, S. Y. Ko, S. Kim, K. M. Choi, W. -H. Ryu, *Small* 19 (2023) 2206561.
40. Y. -S. Lee, K. -S. Ryu, *Sci. Rep.* 17 (2017) 16617.
41. S. H. Lee, C. Huang, P. S. Grant, *Energy Storage Mater.* 33 (2020) 408-415.
42. S. H. Lee, C. Huang, P. S. Grant, *Nano Energy* 61 (2019) 96-103.

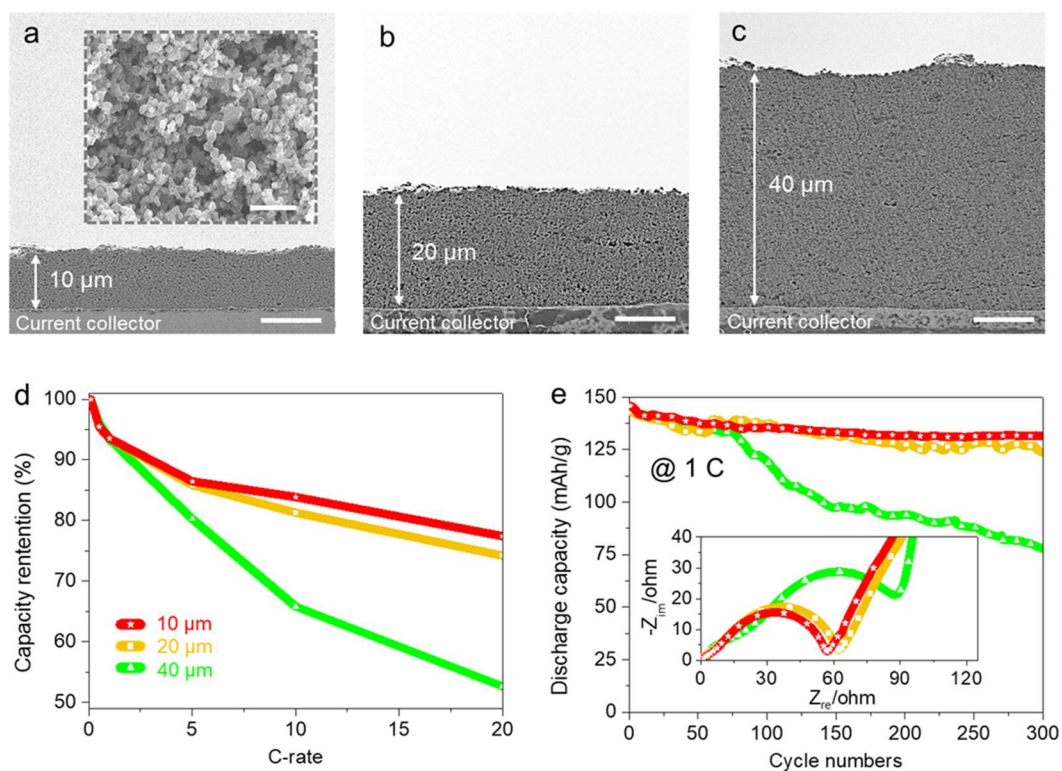


**Figure 1.** SEM images for the cross-sections of the spray-coated LTO electrodes with controlled thickness of (a) 10  $\mu\text{m}$ , (b) 20  $\mu\text{m}$  and (c) 40  $\mu\text{m}$ . The scale bars indicate 10  $\mu\text{m}$ . The inset in Figure 1a represents the magnified view of the electrode surface, and the scale bar indicates 500 nm. (d) Gravimetric discharge capacity retention profiles of the identical electrodes at increasing C-rates in the potential range 1.0 to 2.5 V (vs.  $\text{Li}/\text{Li}^+$ ). (e) Galvanostatic discharge capacity plots at a constant charge/discharge rate of 1 C in the potential range 1.0 to 2.5 V (vs.  $\text{Li}/\text{Li}^+$ ). The inset shows the Nyquist curves for the same electrodes.

**Table 1.** Summary data for the spray-coated LTO electrodes as a function of the electrode mass loading and thickness.

Electrode type	Mass loading (mg/cm <sup>2</sup> )	Thickness ( $\mu$ m)	Discharge capacity (mAh/g)			
			0.1 C	1 C	10 C	20 C
10 $\mu$ m LTO	1.15 $\pm$ 0.04	10 $\pm$ 1	155	145	130	120
20 $\mu$ m LTO	2.31 $\pm$ 0.04	20 $\pm$ 1	155	145	125	115
40 $\mu$ m LTO	4.65 $\pm$ 0.03	40 $\pm$ 3	154	142	100	80

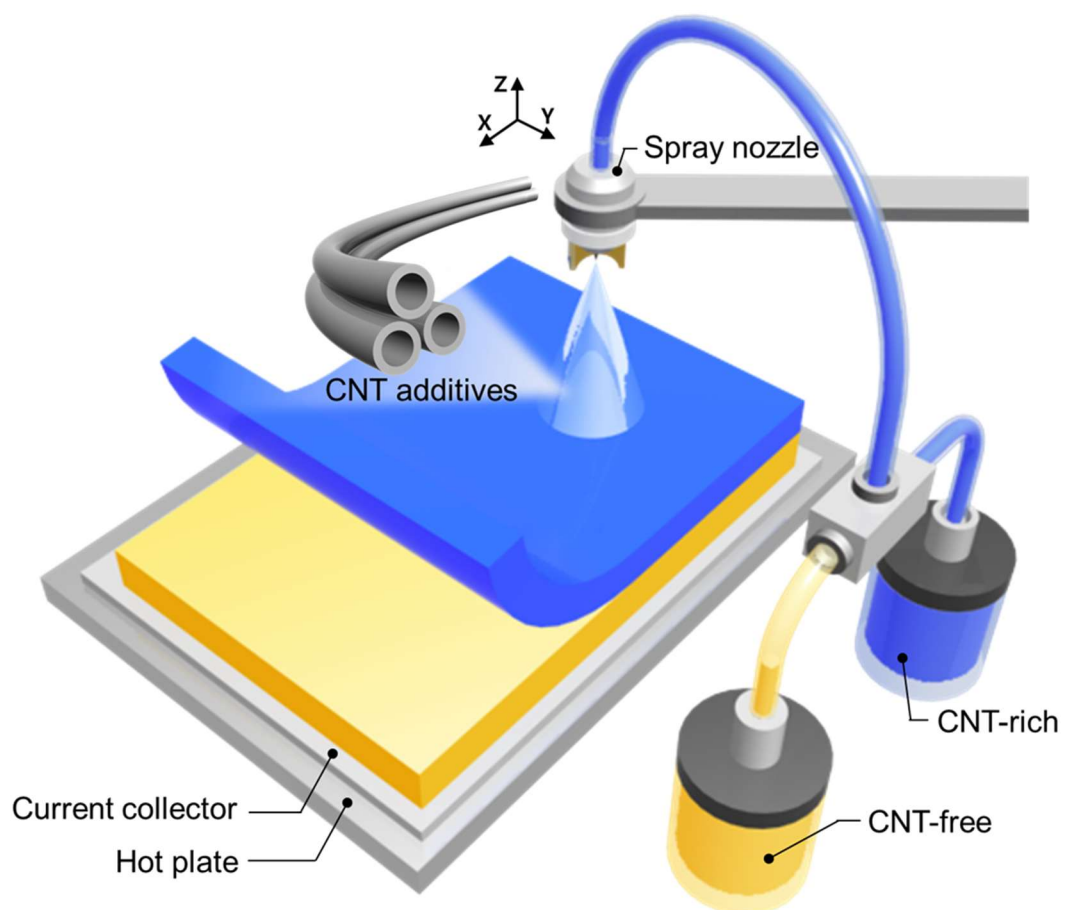


**Figure 2.** Graphical illustration depicts the fabrication of multi-layer architectures using spray coating of sequential, discrete CNT-rich and CNT-free LTO electrodes.

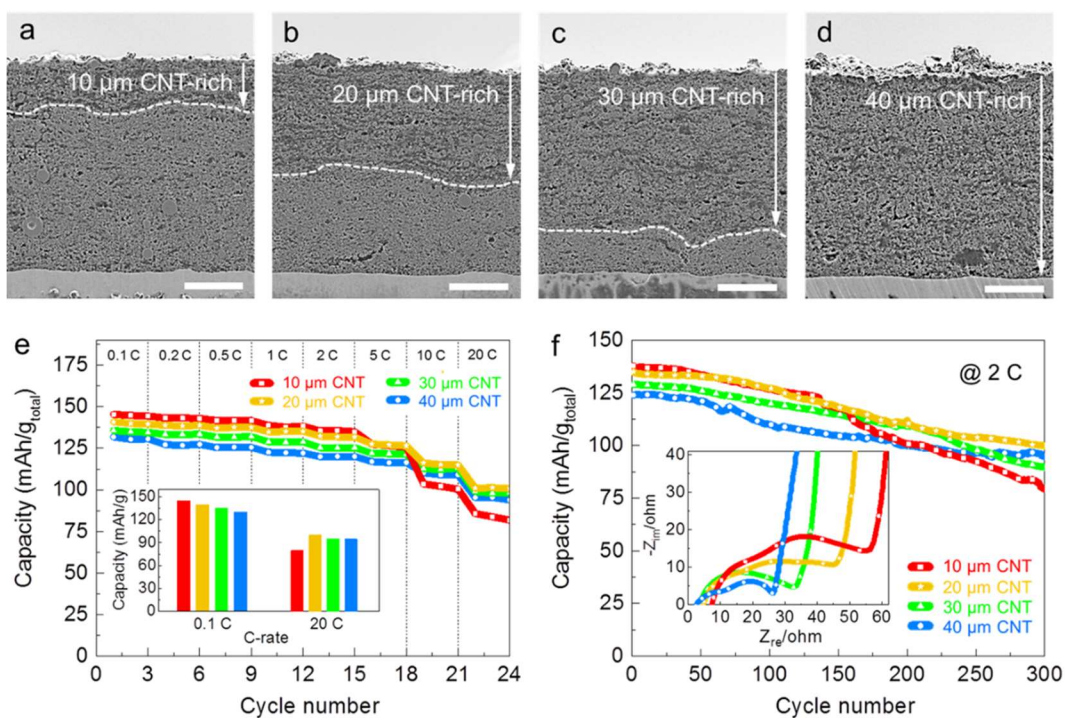


**Figure 3.** SEM images for the cross-section of 40 μm LTO-based electrodes as a function of the CNT-rich layer thickness: (a) 10 μm; (b) 20 μm; (c) 30 μm; and (d) 40 μm. The scale bars indicate 10 μm. (e) Gravimetric discharge capacity profiles of the identical electrodes at increasing C-rate in the potential range 1.0 to 2.5 V (vs. Li/Li<sup>+</sup>). The inset bar graph summarizes the discharge capacity tendency at 0.1 C and 20 C. (f) Galvanostatic discharge capacity plots at a constant charge/discharge rate of 2 C in the potential range 1.0 to 2.5 V (vs. Li/Li<sup>+</sup>). The inset indicates the Nyquist curves for the same electrodes.

**Table 2.** Summary data for 40  $\mu\text{m}$  LTO-based electrodes with differing the thickness of CNT-rich layers.

Electrode Type	Mass loading ( $\text{mg}/\text{cm}^2$ )	Thickness ( $\mu\text{m}$ )	Discharge capacity ( $\text{mAh}/\text{g}$ )			
			0.1 C	1 C	10 C	20 C
10 $\mu\text{m}$ CNT	$4.63 \pm 0.04$	$40 \pm 1$	145	140	100	80
20 $\mu\text{m}$ CNT	$4.64 \pm 0.04$	$40 \pm 2$	140	135	120	100
30 $\mu\text{m}$ CNT	$4.63 \pm 0.05$	$40 \pm 2$	135	130	115	95
40 $\mu\text{m}$ CNT	$4.65 \pm 0.05$	$40 \pm 3$	130	125	110	90

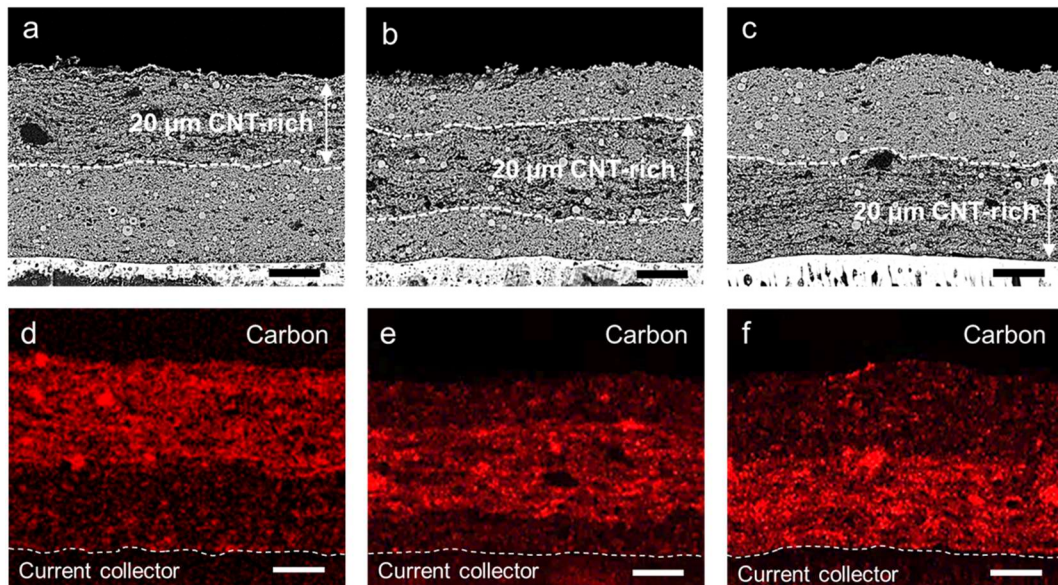


**Figure 4.** CBS images for the cross-section of the 40  $\mu\text{m}$  multi-layers according to the spatial variation of 20  $\mu\text{m}$  CNT-rich layers: (a) on the top of the LTO-only layer (LTO-CNT); (b) between two layers of LTO-only (LTO-CNT-LTO); and (c) at the base of the LTO-only layer (CNT-LTO). (d-f) Corresponding EDS elemental map images (for carbon) for the identical multi-layer structures. All the scale bars indicate 10  $\mu\text{m}$ .

**Table 3.** Summary data for the multi-layers with varying the location of CNT-rich layers.

Electrode Type	Thickness ( $\mu\text{m}$ )	Mass loading ( $\text{mg}/\text{cm}^2$ )	Discharge capacity ( $\text{mAh}/\text{g}$ )			
			0.1 C	1 C	10 C	20 C
CC    LTO-CNT	$40 \pm 2$	$4.62 \pm 0.04$	140	134	120	100
CC    LTO-CNT-LTO	$40 \pm 2$	$4.61 \pm 0.05$	140	132	110	95
CC    CNT-LTO	$41 \pm 3$	$4.62 \pm 0.05$	140	130	100	85

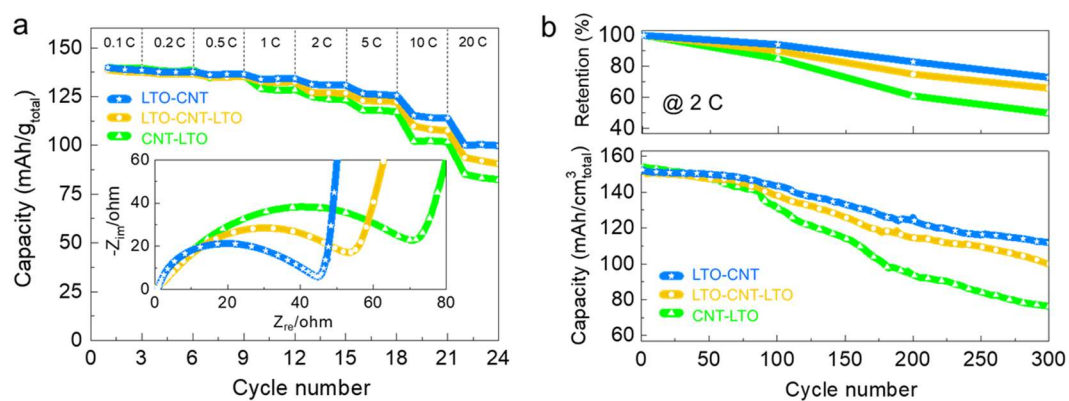


**Figure 5.** (a) Gravimetric discharge capacity profiles at increasing C-rate in the potential range 1.0 to 2.5 V (vs. Li/Li<sup>+</sup>). The inset shows the Nyquist curves for the identical multi-layer electrodes. (b) Galvanostatic volumetric discharge capacity plots at a constant charge/discharge rate of 2 C (lower) and the corresponding capacity retention profiles (upper).

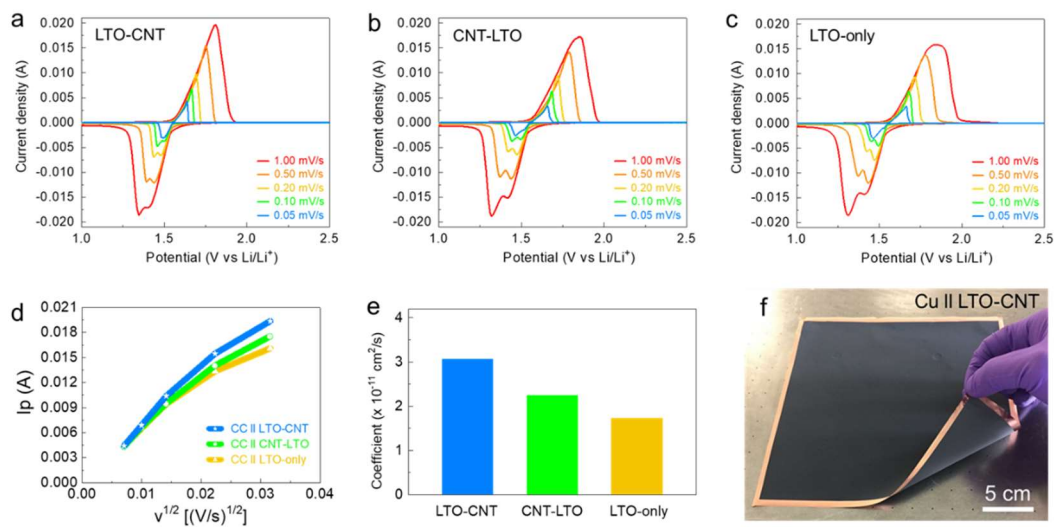


**Figure 6.** (a-c) CV profiles for the LTO-CNT, CNT-LTO and LTO-only electrodes at increasing scan rates of 0.05 to 1.0 mV/s in the potential range 1.0 to 2.5 V (vs. Li/Li<sup>+</sup>). (d) The linear relationship between the anodic peak current density at approximately 1.7 V and the square root of the scan rate for the identical electrodes. (e) Corresponding effective lithium ion mobility estimates. (f) The photograph for the spray-coated double-sided LTO-CNT multi-layer over a 20 cm × 20 cm Cu current collector.

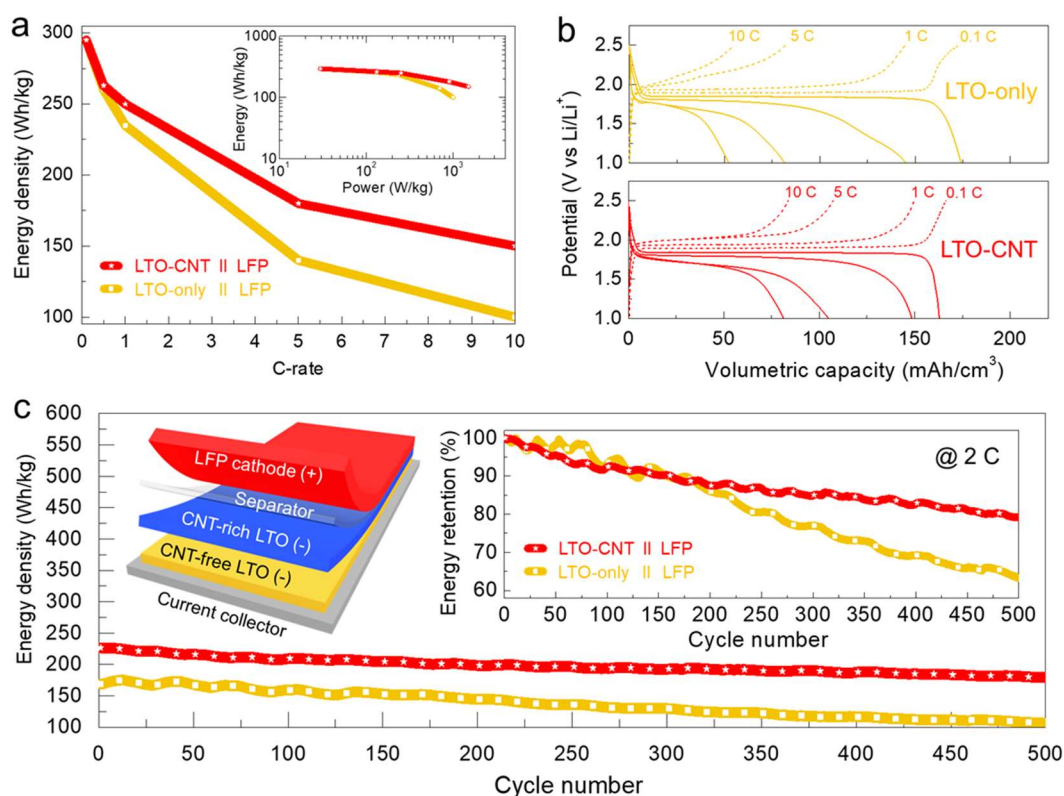
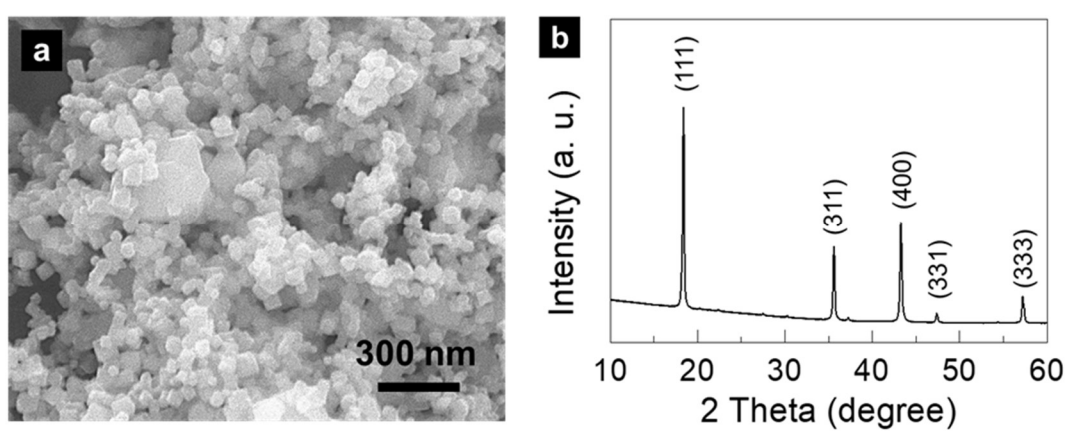


**Figure 7.** (a) Gravimetric discharge energy density profiles at increasing C-rates in the voltage window 1.0 to 2.5 V (vs.  $\text{Li/Li}^+$ ) for the LTO-CNT and LTO-only LIB configurations. The inset shows corresponding Ragone plots. (b) Comparative volumetric charge/discharge curves for the same LIBs. (c) Galvanostatic discharge energy density plot at 2 C. The right-hand inset shows the corresponding energy density retention, and the left-hand illustration depicts the best performing LTO-CNT || LFP LIB arrangement.

**Table 4.** Summary data for LIB configurations with differing LTO-based negative electrode types.

LIB Type	Electrode mass loading (mg/cm <sup>2</sup> )		Gravimetric discharge capacity (mAh/g)			
	Anode	Cathode	0.1 C	1 C	5 C	10 C
LTO-CNT    LFP	4.62 ± 0.05	4.76 ± 0.04	150	124	70	48
LTO-only    LFP	4.63 ± 0.04	4.77 ± 0.04	152	130	90	70

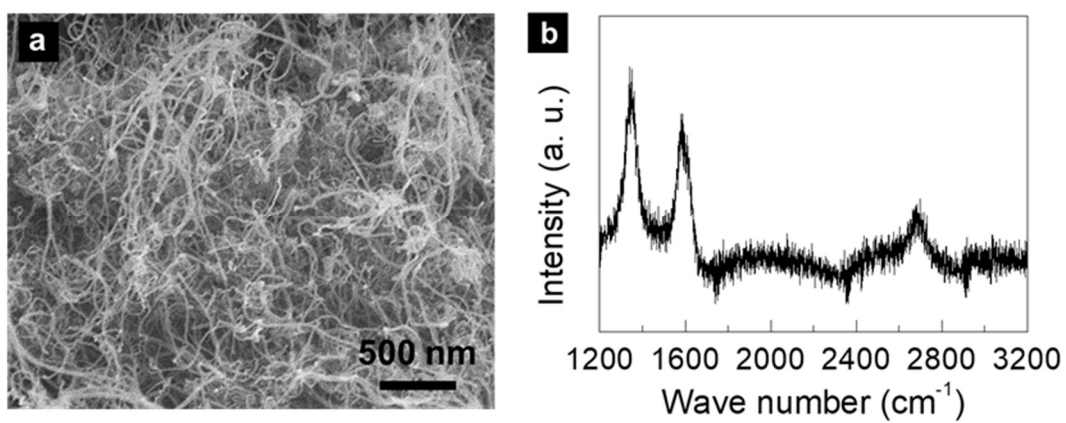
# Supporting Information



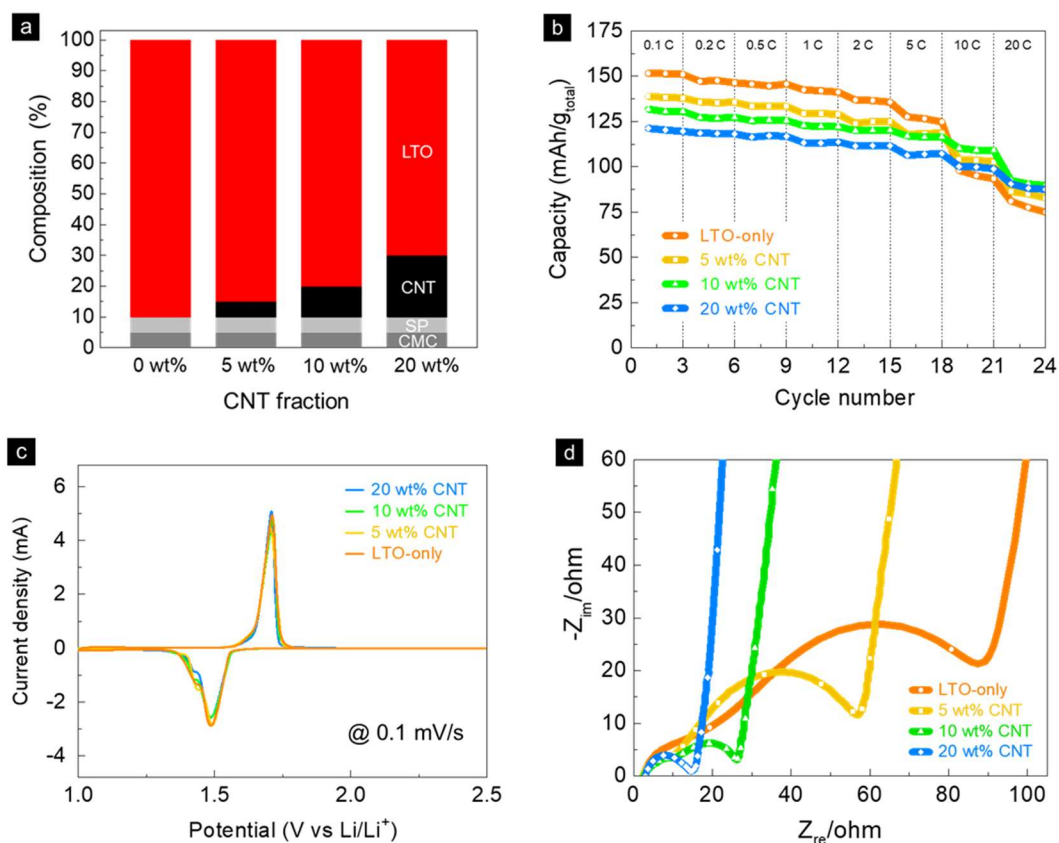
**Figure S1.** (a) SEM image and (b) XRD patterns for pristine LTO particles.



**Figure S2.** The photograph shows the CNT-rich LTO suspension, providing visual evidence of the suspension's stability with no solid electrode constituent settling or forming sediment.



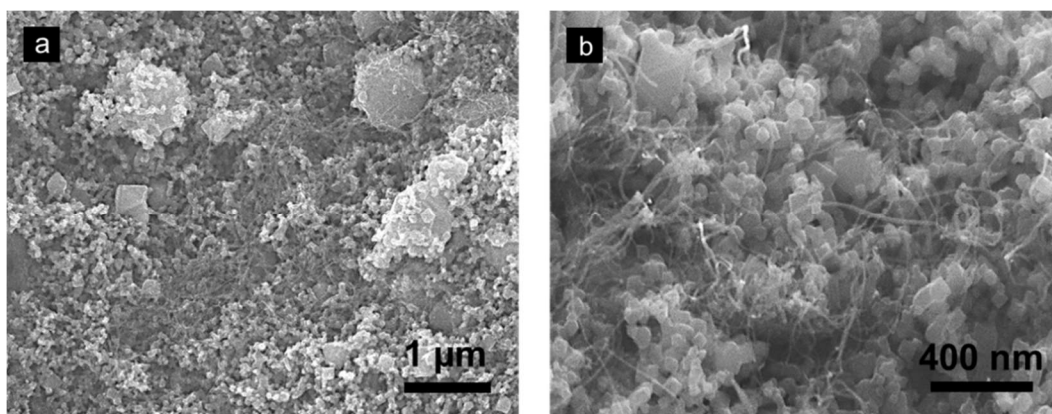
**Figure S3.** (a) SEM image and (b) Raman data for multi-wall CNT structures.



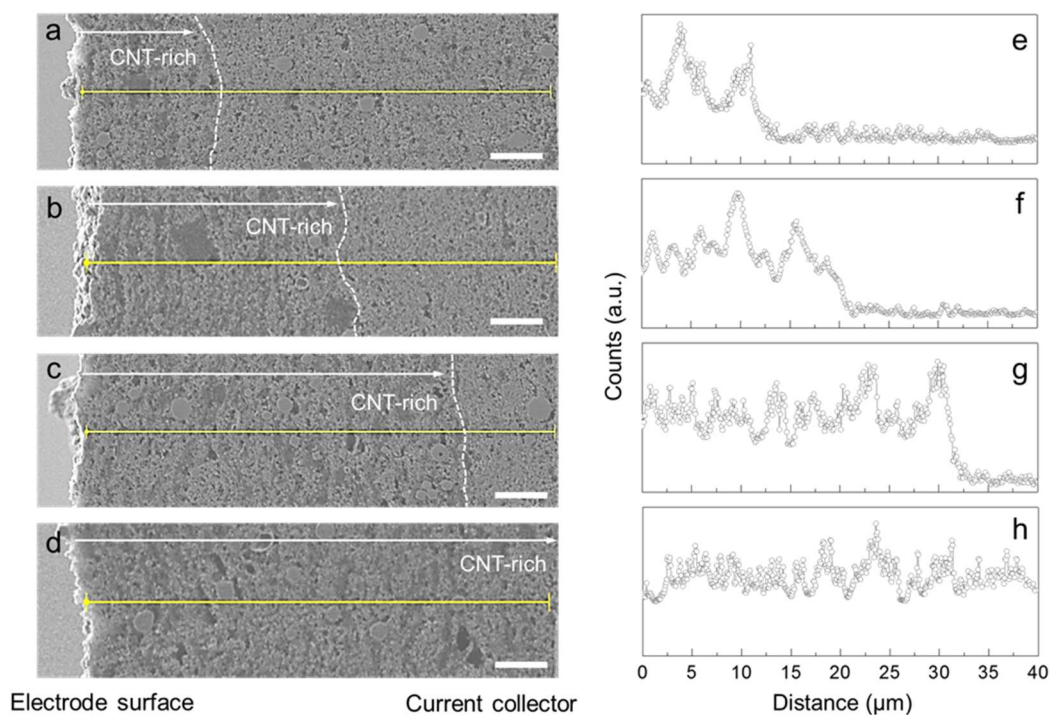
**Figure S4.** (a) The comparative bar graphs show the variation of CNT fractions within the 40  $\mu\text{m}$  spray-coated LTO electrodes, in a range of 0 to 20 wt%. (b) Gravimetric discharge capacity profiles of spray-coated LTO electrodes as a function of CNT fractions at increasing C-rates in the potential range 1.0 to 2.5 V (vs. Li/Li<sup>+</sup>). (c) CV profiles at 0.1 mV/s in the potential range 1.0 to 2.5 V (vs. Li/Li<sup>+</sup>) for the same electrodes. (d) The corresponding Nyquist curves.

**Table S1.** Summary data for LTO-based electrodes with varying CNT fractions.

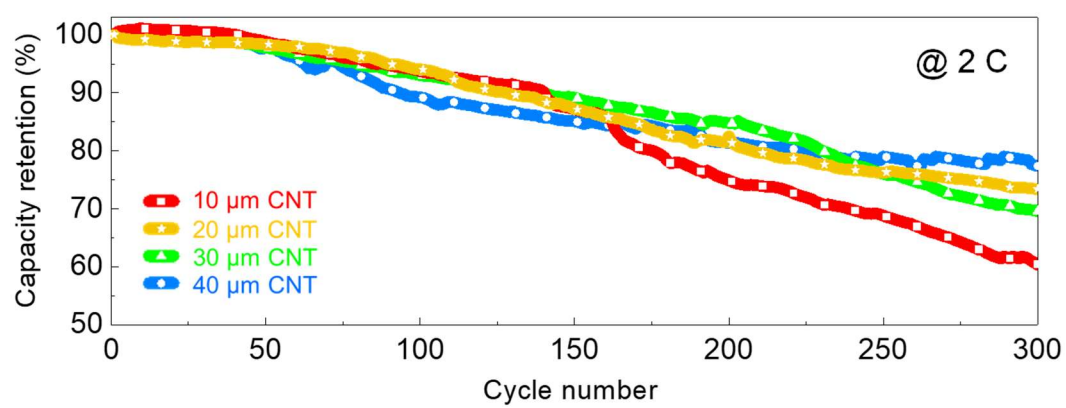
Electrode Type	Formulation (LTO:CNT:SP:CMC)	Mass loading (mg/cm <sup>2</sup> )	Discharge capacity (mAh/g)			
			0.1 C	1 C	10 C	20 C
LTO-only	90 : 0 : 5 : 5	4.65 ± 0.03	154	142	100	80
5 wt% CNT	85 : 5 : 5 : 5	4.64 ± 0.04	140	130	108	85
10 wt% CNT	80 : 10 : 5 : 5	4.62 ± 0.04	130	123	110	95
20 wt% CNT	70 : 20 : 5 : 5	4.61 ± 0.05	120	115	105	90



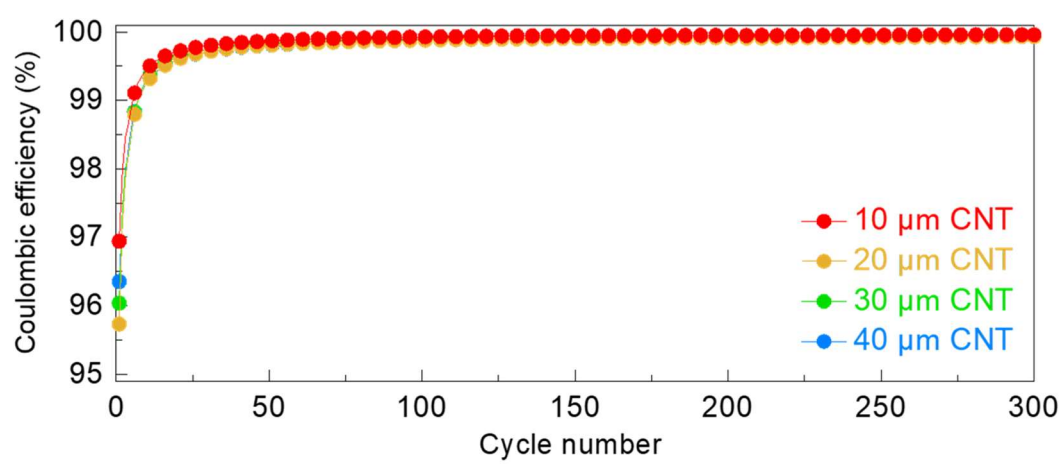
**Figure S5.** (a) SEM image for the surface of the spray-coated LTO electrode with 10 wt% CNT additives. (b) The magnified SEM image for the region of CNT agglomerates, representing that CNTs were entangled with particulates of LTO and SP.



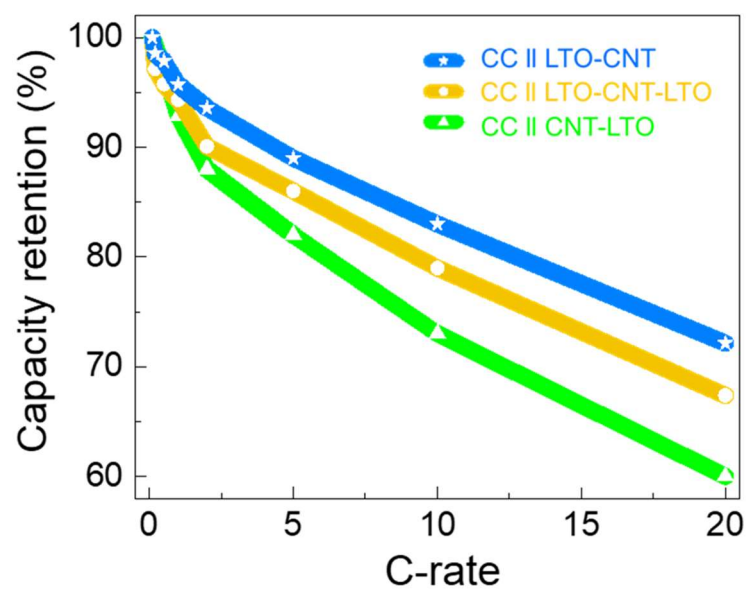
**Figure S6.** A series of SEM images for the cross-section of the 40  $\mu\text{m}$  multi-layers with the controlled thickness of the CNT-rich layer: (a) 10  $\mu\text{m}$ ; (b) 20  $\mu\text{m}$ ; (c) 30  $\mu\text{m}$ ; and (d) 40  $\mu\text{m}$ . All the scale bars indicate 5  $\mu\text{m}$ . (e-h) Corresponding EDS line scanning profiles (for carbon) across the through-thickness multi-layer electrodes, starting from the electrode surface to the current collector.



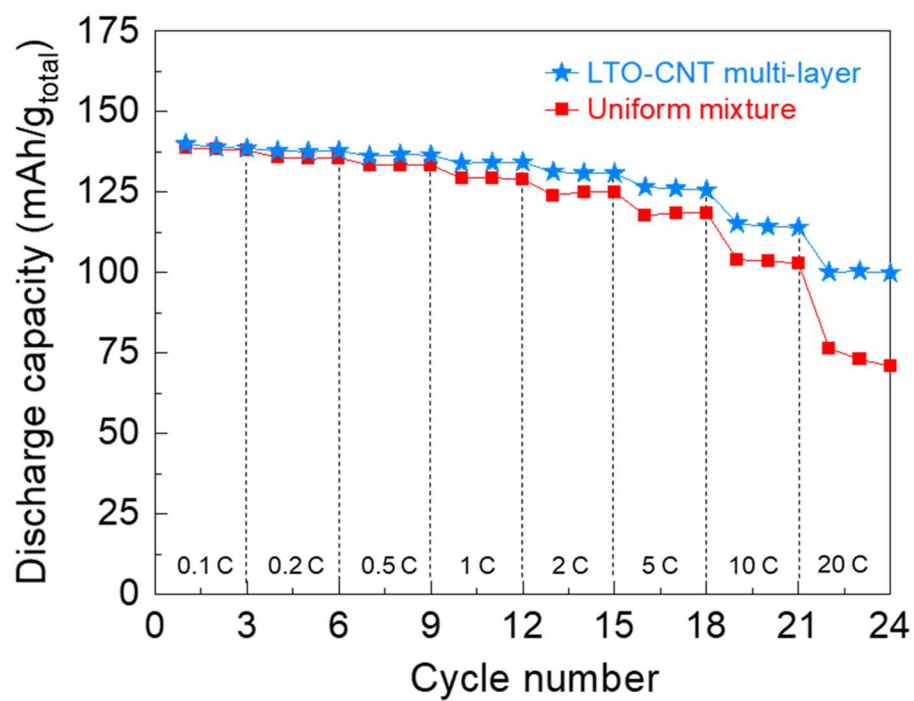
**Figure S7.** Corresponding capacity retention profiles for the galvanostatic discharge cycles in Figure 3f.



**Figure S8.** Corresponding coulombic efficiency profiles for the galvanostatic discharge cycles in Figure 3f.



**Figure S9.** Corresponding capacity retention profiles for the discharge capacity tendency at increasing C-rates in Figure 5a.



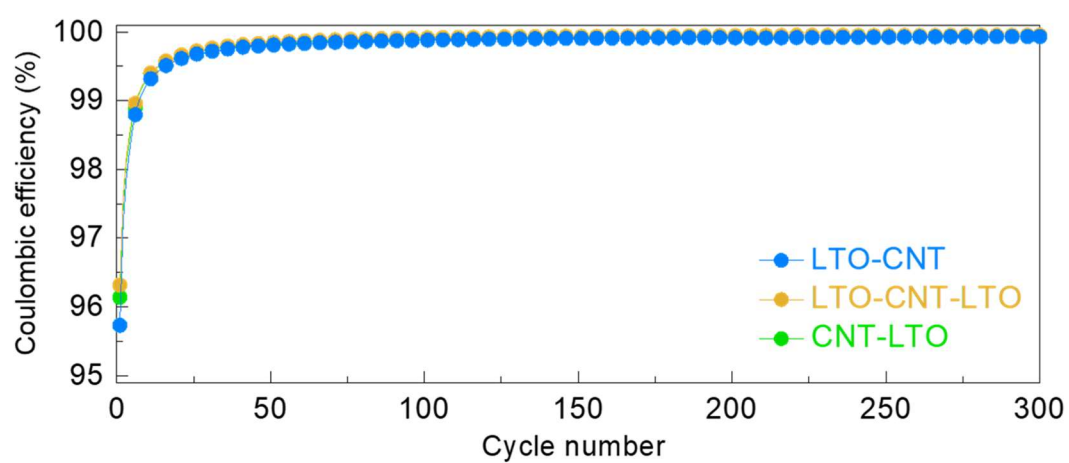


**Figure S11.** Corresponding coulombic efficiency profiles for the volumetric discharge cycles in Figure 5b.

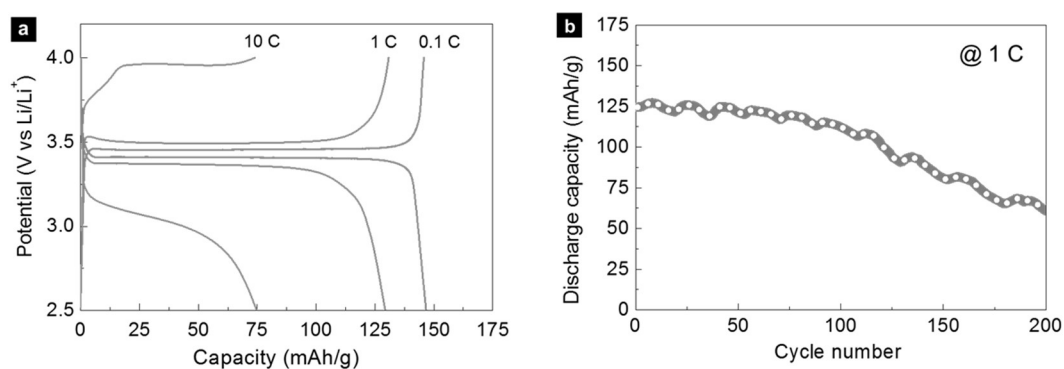


**Figure S12.** (a) Gravimetric charge/discharge profiles of spray-coated LFP electrodes at increasing C-rates in the potential range 2.5 to 4.0 V (vs. Li/Li<sup>+</sup>). The LFP electrodes were fabricated over Al current collector foils, which were formulated with a 90:5:5 mass ratio of LFP:SP:CMC without CNT additives. (b) Galvanostatic discharge capacity plots at a constant rate of 1 C in the potential range 2.5 to 4.0 V (vs. Li/Li<sup>+</sup>) for the spray-coated LFP electrode.

**Table S2.** Summary data for the spray-coated LFP positive electrode.

Formulation (LFP : SP : CMC)	Mass loading (mg/cm <sup>2</sup> )	Thickness (μm)	Discharge capacity (mAh/g)		
			0.1 C	1 C	10 C
90 : 5 : 5	4.81 ± 0.04	44 ± 4	150	130	75